








RESEARCH ARTICLE | JANUARY 29 2024

## X-ray absorption spectroscopy and theoretical investigations of the effect of extended ligands in potassium organic matter interaction

Jocelyn A. Richardson ; Hoshin Kim ; Joshua J. Kas ; Xiao You; Amity Andersen ; Bojana Ginovska ; Arunima Bhattacharjee ; Ritimukta Sarangi  

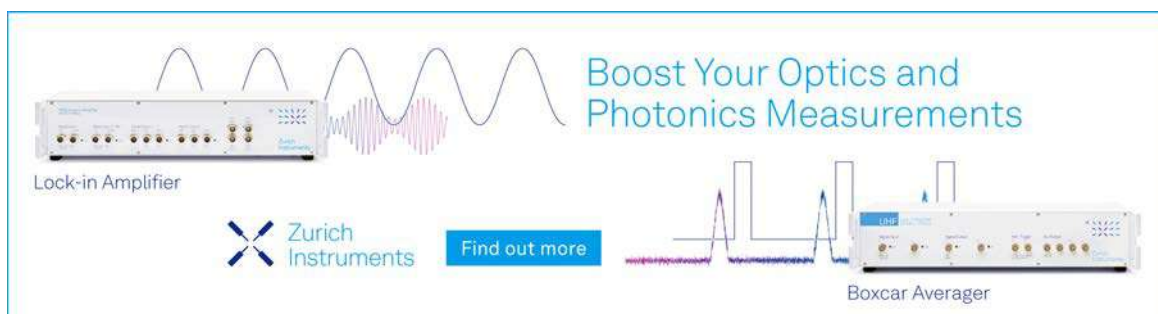


*J. Chem. Phys.* 160, 044114 (2024)

<https://doi.org/10.1063/5.0183603>




CrossMark



Boost Your Optics and Photonics Measurements

Lock-in Amplifier

 Zurich Instruments

[Find out more](#)

Boxcar Averager

# X-ray absorption spectroscopy and theoretical investigations of the effect of extended ligands in potassium organic matter interaction

Cite as: *J. Chem. Phys.* **160**, 044114 (2024); doi: [10.1063/5.0183603](https://doi.org/10.1063/5.0183603)

Submitted: 23 October 2023 • Accepted: 7 January 2024 •

Published Online: 29 January 2024



View Online



Export Citation



CrossMark

Jocelyn A. Richardson,<sup>1</sup> Hoshin Kim,<sup>2</sup> Joshua J. Kas,<sup>3</sup> Xiao You,<sup>1</sup> Amity Andersen,<sup>4</sup> Bojana Ginovska,<sup>2</sup> Arunima Bhattacharjee,<sup>4</sup> and Ritimukta Sarangi<sup>1,a)</sup>

## AFFILIATIONS

<sup>1</sup>Stanford Synchrotron Radiation Lightsource, SLAC National Accelerator Laboratory, 2575 Sand Hill Road, Menlo Park, California 94025, USA

<sup>2</sup>Physical Sciences Division, Physical and Computational Sciences Directorate, Pacific Northwest National Laboratory, 902 Battelle Blvd., Richland, Washington 99354, USA

<sup>3</sup>Department of Physics, University of Washington Seattle, Box 351560, Seattle, Washington 98195, USA

<sup>4</sup>Environmental Molecular Sciences Division, Earth and Biological Sciences Directorate, Pacific Northwest National Laboratory, 3335 Innovation Blvd., Richland, Washington 99354, USA

<sup>a)</sup>Author to whom correspondence should be addressed: [ritis@slac.stanford.edu](mailto:ritis@slac.stanford.edu)

## ABSTRACT

Potassium (K) is an essential nutrient for plant growth, and despite its abundance in soil, most of the K is structurally bound in minerals, limiting its bioavailability and making this soil K reservoir largely inaccessible to plants. Microbial biochemical weathering has been shown to be a promising pathway to sustainably increase plant available K. However, the mechanisms underpinning microbial K uptake, transformation, storage, and sharing are poorly resolved. To better understand the controls on microbial K transformations, we performed K K-edge x-ray absorption near-edge structure (XANES) spectroscopy on K-organic salts, including acetate, citrate, nitrate, oxalate, and tartrate, which are frequently observed as low molecular weight organic acids secreted by soil microbes, as well as humic acid, which acts as a proxy for higher molecular weight organic acids. The organic salts display feature-rich K XANES spectra, each demonstrating numerous unique features spanning ~13 eV range across the absorption edge. In contrast, the spectra for humic acid have one broad, wide feature across the same energy range. We used a combination of time-dependent density functional theory and the Bethe–Salpeter equation based approach within the OCEAN code to simulate the experimental spectra for K-nitrate (KNO<sub>3</sub>) and K-citrate [K<sub>3</sub>(C<sub>6</sub>H<sub>5</sub>O<sub>7</sub>)·H<sub>2</sub>O] to identify the electronic transitions that give rise to some of the outlying and unique spectral features in the organic salts. KNO<sub>3</sub> has both the lowest and highest lying energy features, and K<sub>3</sub>(C<sub>6</sub>H<sub>5</sub>O<sub>7</sub>)·H<sub>2</sub>O is produced by several soil microbes and is effective at mineral weathering. Our results analyze the K-organic salt bonding in detail to elucidate why the spectral shapes differ and indicate that the K K-edge XANES spectra are associated with the entire ligand despite similar first-shell bonding environments around the K center. The improved understanding of K bonding environments with organic ligands and their use for interpretation of the K-XANES spectra provides an important toolkit to understand how K is transformed by microbial processes and made bioavailable for plant uptake.

Published under an exclusive license by AIP Publishing. <https://doi.org/10.1063/5.0183603>

## I. INTRODUCTION

Potassium in its monovalent form (K) is an essential nutrient for plants and plays a central role in regulating the movement of water, nutrients, and carbohydrates through plant tissue and is important for enzyme activation, which influences protein and ATP production.<sup>1–3</sup> In several plant species, K is also critical to

drought stress tolerance.<sup>4–6</sup> Despite these requirements, K is often a limiting nutrient in many earth surface environments primarily due to the lack of soluble (i.e., K<sup>+</sup>) species, where a majority of soil K is bound within mineral phases,<sup>7,8</sup> which is inaccessible to plants. Although commercial K fertilizers are globally available, many farmlands are persistently deficient in K<sup>9</sup> because the input of K fertilizer does not meet the amount of K removed via

harvesting of plants, resulting in a net imbalance of K in most agricultural soils.<sup>10,11</sup>

Mineral weathering and secondary mineral formation are pathways to increase the pool of readily exchangeable and soluble bioavailable K<sup>+</sup> from the mineral bound pool (which is typically non-bioavailable). Both bacteria and fungi have been shown to impact K-rich mineral weathering and dissolution rates and show promise as a sustainable and economic route to increase soluble bioavailable plant K<sup>+</sup>.<sup>11–19</sup> Fungi are known to weather soil minerals by direct or indirect mechanisms, such as a mechanical force<sup>20</sup> and respiration and organic exudates.<sup>20–22</sup> Organic acid exudates, such as oxalic and citric acids, have been observed to play key roles in fungal-mediated processes, including pathogenesis and metal tolerance<sup>12,21,23–25</sup> and the rate of mineral dissolution.<sup>26–28</sup> Various fungal species also produce acetic, tartaric, malic, and fumaric acids.<sup>28–30</sup> Although the presence of fungi has indicated degradation of mineral surfaces<sup>15,31</sup> and increased bulk K in plants in the presence of K minerals,<sup>16,19,32</sup> little is known about the molecular mechanisms controlling these processes.

Molecular characterization techniques, such as X-ray Absorption Near-Edge Structure (XANES) spectroscopy, have the capacity to identify element-specific coordination environments, geometries, and electronic transitions in complex biological samples. This is particularly so in cases with fundamental research explaining the root source of spectroscopic features and with extensive spectroscopic databases for both inorganic and organic compounds. In complex samples, experimental XANES spectra may often reflect mixtures of various chemistries of an element. Mixtures can be deconvolved by linear combination fitting (LCF) of database standards to the experimental spectra of the unknown complex species. Synchrotron x-ray microprobe beamlines have the capability of combining X-ray Fluorescence ( $\mu$ -XRF) imaging with  $\mu$ -XANES spectroscopy, which allows for the characterization of chemical species at the  $\mu$ m scale within complex and heterogeneous samples. However, K  $\mu$ -XRF imaging and XANES spectroscopy studies are limited, and the available published K K-edge XANES spectra are focused on K geometry in mica and silicate minerals,<sup>33–36</sup> catalysts,<sup>37,38</sup> and alkali-ion batteries.<sup>39</sup>

More recently, K K-edge XANES spectroscopy datasets for K minerals and salts have been published in the context of understanding K in environmental samples.<sup>40–42</sup> Although this improves the ability to track K transformations in the rhizosphere, these studies lack extensive K-organic materials, which are critical to understanding the bioavailable K<sup>+</sup> pool and biological transport of K across the plant–rhizosphere microbiome. To better understand the transformations between soil and fungal K,<sup>43</sup> we measured K K-edge XANES spectra for several K-organic salts. In addition to a starting database for organic K studies, we detail the electronic transitions that give rise to the spectral features of K-nitrate (KNO<sub>3</sub>) and K-citrate [K<sub>3</sub>(C<sub>6</sub>H<sub>5</sub>O<sub>7</sub>)·H<sub>2</sub>O] by combining XANES spectroscopy with computational approaches. Understanding the electronic transitions that result in the features observed in KNO<sub>3</sub> is broadly applicable to other K-organic compounds since KNO<sub>3</sub> has both the lowest and highest energy features of the standard materials measured, bracketing the energy range of the electronic transitions in the selected standards. Citric acid is known to play a role in microbially mediated mineral degradation and has been observed in the XANES spectra from within the fungal biomass of hyphae.<sup>44</sup> Therefore,

understanding the electronic transitions in K<sub>3</sub>(C<sub>6</sub>H<sub>5</sub>O<sub>7</sub>)·H<sub>2</sub>O is important to our understanding of K uptake and storage by fungi.

X-ray Absorption Spectroscopies (XAS) are often combined with various computational methods. Such methods include time-dependent density functional theory (TD-DFT), multiple-scattering based theories (FEFF and MXAN), Bethe–Salpeter Equation (BSE) based approaches (OCEAN) combined with molecular dynamics (MD), and DFT methods (QM-MM). These methods have their strengths and weaknesses in simulating different types of systems and selected energy regions of the experimental spectra. For example, local basis set TD-DFT based methods are typically more accurate in simulating transitions to bound states or lower-lying valence molecular states and have the benefit of being all-electron, allowing for accurate prediction of relative edge energies.<sup>45</sup> This is particularly true for small molecules, which can be modeled by localized Gaussian basis function methods and require no periodicity. TD-DFT can also be implemented using plane wave codes, such as implemented in ABINIT, Quantum ESPRESSO, and Vienna *Ab initio* Simulation Package (VASP), making it more appropriate for periodic systems. Meanwhile, multiple scattering-based methods have been more successful in simulating the spectra at or over the continuum (white line and higher energy) and are especially good for calculations at very high energies.<sup>46</sup> Finally, plane wave pseudopotential-based BSE bridges the two, with calculations that are quite accurate for both bound and mid-range continuum energies up to about ~100 eV above the edge. In a recent study, researchers have applied plane wave pseudopotential-based DFT to K XANES spectroscopy of Prussian blue, which was able to simulate up to five features across 20 eV of the K K-edge.<sup>39</sup> The K K-edge occurs at ~3608 eV, which falls in the tender x-ray regime and results in highly resolved experimental spectral shapes compared to higher-energy transition metal systems. This leads to well-defined features in the absorption spectra, making them a good candidate for interpretation using theoretical methods. Since K dominantly forms weak ionic bonds in its monovalent form, the K-organic acid compounds studied here are unlikely to have a strong K-ligand bonding/low-lying bound state transitions. Therefore, a combination of TD-DFT and BSE based methods was applied to understand the K-edge XANES spectra of selected K-organic acid compounds.

## II. MATERIALS AND METHODS

### A. Synchrotron XANES spectroscopy

Potassium K-edge XANES measurements were performed on beamline 14-3 of the Stanford Synchrotron Radiation Lightsource (SSRL), SLAC National Accelerator Laboratory. A water-cooled double Si crystal (111) monochromator was used to select the incident x-ray energy (~3610 eV) and calibrated using the position of the white line of a natural kaolinite powder (Sigma-Aldrich, St. Louis, MO) at 3618.73 eV. Samples were measured in the fluorescence mode using a Vortex ME-7 Si drift detector, under ambient conditions within a helium purged chamber to reduce x-ray attenuation in air. Five samples were used as standard materials in this study: potassium oxalate (K<sub>2</sub>C<sub>2</sub>O<sub>4</sub>), potassium nitrate (KNO<sub>3</sub>), tri-potassium citrate monohydrate [K<sub>3</sub>(C<sub>6</sub>H<sub>5</sub>O<sub>7</sub>)·H<sub>2</sub>O], potassium acetate (KCO<sub>2</sub>Me), and potassium tartrate K<sub>2</sub>(C<sub>4</sub>H<sub>4</sub>O<sub>6</sub>) (Sigma-Aldrich). Humic acid (technical, Sigma-Aldrich) was also measured, but since humic acid is a complex mixture of organic matter, it

is not considered a standard. The samples were ground to a fine, homogenized powder using a ceramic mortar and pestle, repeating the grinding process three times, and a small amount of powder was placed as a fine layer onto sulfur-free tape (Saint-Gobain). This process is at the limit of sample preparation, and it is possible that the grain size of the sample powder was not small enough to completely mitigate self-absorption. Each sample was measured with a  $1 \times 1 \text{ mm}^2$  x-ray beam, and three repeat XANES spectra were obtained per sample. The repeat XANES spectra were averaged using SIXPack.<sup>47</sup> The spectra were then normalized in Athena<sup>48</sup> by applying a linearized pre-edge and a third-order polynomial to the post-edge.

## B. Density functional theory

### 1. Preparation of initial structures of K-organic salts and K-water

The initial structures of  $\text{K}_3(\text{C}_6\text{H}_5\text{O}_7) \cdot \text{H}_2\text{O}$  were obtained from the Cambridge Structural Database (CSD),<sup>49</sup> and  $\text{KNO}_3$  structures were obtained from the Crystallography Open Database (C.O.D.)<sup>50</sup> (Fig. S1). Classical MD simulations were used to obtain representative geometries of a potassium ion solvated in water for use in the TD-DFT and BSE spectra calculations. A potassium ion was placed in the center of a cubic periodic box ( $4.04 \times 4.04 \times 4.04 \text{ nm}^3$ ) with 6492 water molecules. The TIP3P water model<sup>51</sup> was used, along with parameters for the potassium monovalent ion developed by Joung and Cheatham.<sup>52</sup> For the MD simulations, we used the GROMACS version 2018.6 MD program.<sup>53</sup> The initial system was minimized using the steepest descent algorithm up to a maximum residual force of  $10 \text{ kJ}^{-1} \text{ mol}^{-1} \text{ \AA}^{-1}$ . Then, the system was optimized for 500 ps under a constant-temperature, constant-volume (NVT) ensemble with the Berendsen velocity rescaling method.<sup>54</sup> Subsequently, it was equilibrated for 500 ps under a constant-temperature, constant-pressure (NPT) ensemble with the Berendsen pressure coupling. After minimization and equilibration, the system was simulated for 100 ns with a time step of 2 fs. Long-range electrostatic interactions were represented using the particle mesh Ewald (PME) method.<sup>55</sup> The hydrogen atoms in the water molecules were constrained using the Linear Constraint Solver (LINCS).<sup>56</sup> Clustering analysis was performed on the structures obtained from the MD simulations, and the representative static geometries of a potassium ion with one to eight water molecules that surround  $\text{K}^+$  were selected for the TD-DFT calculations. The representative conformations were identified by assessing the root-mean-square deviation of the K-water complex with the Gromos algorithm implemented in GROMACS.<sup>53</sup> All analyses, including extracting simulations with  $\text{K}^+$  with one and eight water molecules based on the closest distance and clustering analysis, were performed by the CPPTRAJ module in AmberTools.<sup>57,58</sup> The MD simulations were not applied for K-organic salts because their crystal structures were available from the databases, and the coordinates from these databases were used as inputs for TD-DFT calculations.

### 2. Spectra calculations using TD-DFT

The coordinates from the MD simulations for K-water (see above) (Fig. S2) were used for geometry optimizations using the DFT as implemented in NWChem. Coordinates for all initial structures for the K-organic salts were obtained from structure databases

(Fig. S2). All initial structures were then modified by Discovery Studio Visualizer<sup>59</sup> to center the coordinate on the potassium ion. All calculations were carried out using the NWChem chemistry code version 7.0.1.<sup>60</sup> The initial geometries were optimized with the PBE0 functional<sup>61</sup> augmented with Grimme's dispersion corrections<sup>62</sup> and Sapporo TZP<sup>63,64</sup> for a potassium ion and cc-PVTZ basis set<sup>65</sup> for C, H, O, and N atoms. After the geometry optimizations, TD-DFT calculations with random-phase approximation (RPA) were subsequently performed to calculate the spectra and compare with experimental data. A total of 68, 160, 785, and 500 were calculated for K with 1 water, K with 8 water, K-acetate, and K-citrate, respectively. All the spectra were then reconstructed from these roots by the Lorentzian function with full width at half maximum (FWHM) of two or more energy spacing. Since DFT does a poor approximation of the core potentials, the calculated spectra were shifted by 77 eV to align with the experimental results. All TD-DFT outputs generated by NWChem were analyzed using the Chemission software.<sup>66</sup>

### 3. Bethe-Salpeter equation calculations

The x-ray absorption spectra were calculated by solving the BSE using OCEAN 3.<sup>67</sup> Within OCEAN, DFT is used to solve for the single particle states and their energies, which are then used as a particle-hole basis to solve the BSE. Within the BSE, the spectrum is written in terms of a particle-hole Green's function,

$$\mu(\omega) = \text{Im} \left( \left\langle \hat{T}^\dagger [E_I + \omega - \hat{H} + i\delta]^{-1} \hat{T} \right\rangle I \right), \quad (1)$$

where  $\omega$  is the incoming photon energy,  $|I\rangle$  denotes the ground state of the system,  $E_I$  denotes the ground state energy,  $\hat{T}$  is a transition operator, usually limited to dipole plus quadrupole terms for XAS, and  $\delta$  is a positive infinitesimal. Finally,  $\hat{H}$  is the particle-hole Hamiltonian,

$$\hat{H} = \hat{h}_p - \hat{h}_h + \hat{H}_{ph}, \quad (2)$$

where  $\hat{h}_p$  and  $\hat{h}_h$  are the single electron particle and hole Hamiltonian as given by DFT and  $\hat{H}_{ph}$  is the particle-hole interaction term. The underlying DFT calculations were performed with the pseudopotential plane wave code, Quantum ESPRESSO,<sup>68-70</sup> using the local density approximation with the functional of Perdew and Wang.<sup>71</sup> All pseudopotentials were taken from the Pseudo Dojo<sup>72</sup> pseudopotential database. As the unit cells of all the systems investigated were relatively large, only a small number of k-points were necessary for convergence (e.g.,  $2 \times 1 \times 2$  k-point grid for  $\text{KNO}_3$ ). For the solvated potassium model  $\text{K}(\text{H}_2\text{O})_8$ , the cluster was placed in a  $20 \times 20 \times 20$  Bohr box, and the calculation was performed using only the  $\Gamma$  point. For all calculated spectra, a Lorentzian broadening of 0.68 eV was applied, corresponding approximately to the core-hole lifetime broadening of K. The spectrum was calculated for all three polarizations, and at all K sites in the unit cell, and averaged to simulate the signal from a powder sample. The edge positions in the simulated spectrum are not reliable, and thus, the energy scale was aligned to each experimental spectrum. In the case of solvated  $\text{K}^+$ , the BSE spectra were aligned to the TD-DFT simulations. Each BSE spectrum was scaled by an arbitrary value to better approximate the intensity of the experimental data. For comparison with the spectrum and analysis of the electronic structure, VASP<sup>73-76</sup> was used to

calculate the angular momentum projected densities of states (DOS) for each of the systems, using the same general settings as were used for the spectrum. For the absorbing potassium site, the  $Z + 1$  approximation was used to approximate the density of states in the presence of the  $1s$  core hole.

### III. RESULTS

#### A. Experimental potassium K-edge XANES

The potassium K-edge XANES probes K  $1s$  to valence through continuum transitions. We have recorded the K K-edge XANES spectroscopy of K-associated organic acids  $\text{KNO}_3$ ,  $\text{K}_2\text{C}_2\text{O}_4$ ,  $\text{K}_2(\text{C}_4\text{H}_4\text{O}_6)$ ,  $\text{KCO}_2\text{Me}$ , and  $\text{K}_3(\text{C}_6\text{H}_5\text{O}_7)\cdot\text{H}_2\text{O}$  (Fig. S1, Table I). Of the available crystal structures for the organic salts, each K is between 5 and 8 coordinated to O in the first shell, with an average

bond distance of  $\sim 2.8$  to  $2.9 \text{ \AA}$  (Table I). Since K is always present as  $\text{K}^+$  and is bonded to O in the first shell at similar coordination and bond distances, the expectation was that these should be similar spectroscopically.

However, the XANES spectra of these organic salts show several unique spectral features [Fig. 1(a)], with as many as five features within 10 eV on and across the edge [Fig. 1(b); Table II], of which humic acid is an exception. Humic acid displays one broad peak, with a maximum intensity at 3618.8 eV, and no other pre- or post-edge features.  $\text{KNO}_3$  and  $\text{KCO}_2\text{Me}$  are richer in spectral features compared to  $\text{K}_3(\text{C}_6\text{H}_5\text{O}_7)\cdot\text{H}_2\text{O}$ ,  $\text{K}_2\text{C}_2\text{O}_4$ , and  $\text{K}_2(\text{C}_4\text{H}_4\text{O}_6)$ .  $\text{KNO}_3$  and  $\text{KCO}_2\text{Me}$  have the lowest energy feature of the samples measured, at  $\sim 3612.2$  eV, as a low energy peak and an inflection on the rising edge, respectively. A feature at 3614.15 eV in  $\text{KCO}_2\text{Me}$  is also present as a shoulder on the rising edge of  $\text{KNO}_3$ ,  $\text{K}_2\text{C}_2\text{O}_4$ ,

TABLE I. Crystal structure information for organic salts.

Sample	Chemical formula	Crystal structure <sup>a</sup>	Co-ordination number	First shell atoms	First shell average bond distance	Second shell atoms	Second shell average bond distance
K-nitrate	$\text{KNO}_3$	C.O.D	6	O	2.88	N	3.53
K-citrate	$\text{K}_3(\text{C}_6\text{H}_5\text{O}_7)\cdot\text{H}_2\text{O}$	Cambridge	6	O	2.85	C, O	3.18
K-tartrate	$\text{K}_2(\text{C}_4\text{H}_4\text{O}_6)$	Cambridge	5	O	2.80	C, O	3.49
K-acetate	$\text{KCO}_2\text{Me}$	Not available	...	...	...	...	...
K-oxalate	$\text{K}_2\text{C}_2\text{O}_4$	Cambridge	8	O	2.84	C, K	3.52
Humic acid	N/A	N/A	...	...	...	...	...

<sup>a</sup>For crystal structures, see Fig. S1.

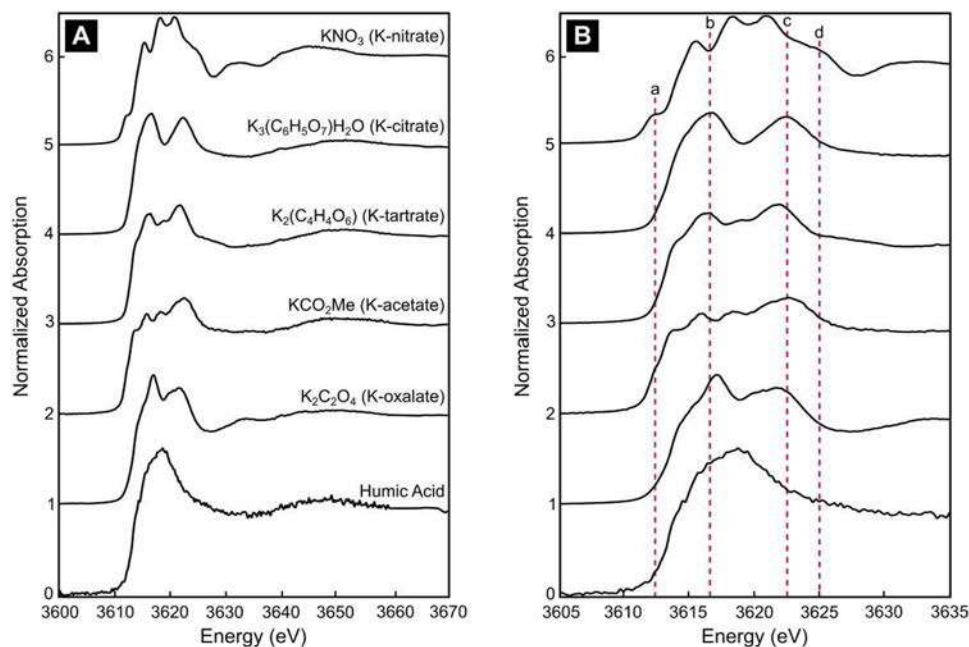


FIG. 1. Potassium k-edge XANES spectroscopy of various organic salts. (a) Stacked K XANES spectra of K organic salts, including humic acid. (b) XANES spectra in (a) (same order) over a shortened energy range to highlight the features unique to each spectrum. The red bars highlight the unique features of interest to be investigated with TD-DFT and BSE, including the highest and lowest energy features within the dataset (both in  $\text{KNO}_3$ ) as well as two prominent features of  $\text{K}_3(\text{C}_6\text{H}_5\text{O}_7)\cdot\text{H}_2\text{O}$  that approximate overlap with features in other XANES spectra. From left to right: (a) 3612.2 eV, (b) 3617.0 eV, (c) 3622.8 eV, and (d) 3625.0 eV.

TABLE II. XANES spectra features and energy positions.

Sample	Pre-edge	Edge features	Immediate post-edge features	Multiple scattering
KNO <sub>3</sub> (K-nitrate)	3612.2	3615.6	3625.0	3645.8
	3614.15	3618.7 3621.1	3632.4	
K <sub>3</sub> (C <sub>6</sub> H <sub>5</sub> O <sub>7</sub> )H <sub>2</sub> O (K-citrate)	...	3617.0 3622.6		3651.6
	3614.15	3616.6 3619.0 3622.1		3651.6
K <sub>2</sub> (C <sub>4</sub> H <sub>4</sub> O <sub>6</sub> ) (K-tartrate)	3612.2	3616.1		3650.0
	3614.15	3618.7 3628.05		
K <sub>2</sub> C <sub>2</sub> O <sub>4</sub> (K-oxalate)	3614.15	3617.2 3622.1	3633.6	3651.6
	Humic acid	...	3618.8	...

and K<sub>2</sub>(C<sub>4</sub>H<sub>4</sub>O<sub>6</sub>). At 3615.6 and 3618.7 eV, there are two separate peaks in both KCO<sub>2</sub>Me and KNO<sub>3</sub>. K<sub>3</sub>(C<sub>6</sub>H<sub>5</sub>O<sub>7</sub>)·H<sub>2</sub>O, K<sub>2</sub>C<sub>2</sub>O<sub>4</sub>, and K<sub>2</sub>(C<sub>4</sub>H<sub>4</sub>O<sub>6</sub>) all have peaks between 3616.6 and 3617.2 eV. A second, similar intensity peak to the previous feature is present within 1 eV of 3622.0 eV of all spectra. Only KNO<sub>3</sub> and K<sub>2</sub>C<sub>2</sub>O<sub>4</sub> show immediate post-edge features, and all spectra show a broad multiple scattering feature between 3645 and 3652 eV.

To determine the source of the unique spectra features, we have combined TD-DFT and BSE theoretical approaches. TD-DFT has strengths within ~5 eV of an absorption edge, is sensitive to short-range molecular orbital (MO) interactions, and can be applied to disordered systems. However, BSE as implemented in OCEAN is based on plane wave basis functions and is thus applicable to features arising from local (bound) states as well as higher energy (continuum) features, yet is more suited to crystalline systems, requiring a supercell to simulate molecules. Combining these approaches provides a robust analysis of the electronic transitions, giving rise to the unique K XANES spectral features.

## B. Theoretical simulations

The K K-edge XAS spectrum for KNO<sub>3</sub> is well simulated by the BSE, replicating five main features around the edge within 1 eV of 3612.0, 3615.6, 3618.7, 3621.3, and 3624.5 eV [Fig. 2(a)]. In addition, BSE simulates a higher energy peak at ~3632.0 eV, although it is narrower and appears to be composed of two transitions compared to one in the experimental spectrum. The potassium p-DOS shows features between 2 and 15 eV that align with the features in the XAS as expected from the electric dipole allowed nature of the x-ray spectral transitions. The s-DOS shows smaller contributions [Fig. 2(c)] consistent with sp hybridization in K resulting from molecular overlap with the ligands. Furthermore, K d-DOS also contributes strongly, but only to the lowest energy features.

This can be attributed to transitions occurring from 1s to 3d levels that are lower in energy relative to the 4p levels. The K d-DOS is included in Fig. S7 of the supplementary material. In KNO<sub>3</sub>, the DOS associated with the nitrate ligand contributes to the transitions labeled i, ii, and v [Figs. 2(a) and 2(c)] (N p-DOS) and to iii and iv (N s-DOS). Interestingly, p-DOS decomposition analysis of NO<sub>3</sub><sup>-</sup> shows that the bidentate coordination of NO<sub>3</sub><sup>-</sup> with K<sup>+</sup> splits the px, py, and pz contributions with the pz contributing to i and ii, while px and py contribute to the higher-energy features (N p-DOS). The sp<sup>2</sup>-like hybridization of the NO<sub>3</sub><sup>-</sup> group results in the out-of-plane N s-pz to be significantly lower in energy relative to the in-plane N s-px and s-py. This orbital mixes with K<sup>+</sup> in KNO<sub>3</sub> and manifests as the outlying low-energy transition in the K K-edge spectra. Thus, while the overall crystal field effects impact longer range structure and bonding, the local ligand field effect can have a significant impact on the energy and intensity of the bound state features. The O DOS is similar to the N DOS, with the exception of O s-DOS, which contributes over a greater energy range than N. Together, the orbital decomposition analysis shows that orbital overlap between K<sup>+</sup> and NO<sub>3</sub><sup>-</sup> directly impacts the K K-edge XAS spectral intensities. To understand this further, TD-DFT calculations were performed to directly correlate spectral shape with MO compositions [Fig. 2(d)]. All five features in the experimental spectrum are reproduced by TD-DFT; however, feature iii is calculated to have very high intensity and deviates from the experiment. This also gives the appearance of lower intensity of the other features in the calculated spectrum. The lowest energy feature in KNO<sub>3</sub> is a result of N and O molecular orbital hybridization with K (4p), with approximately equal contributions from N and O [Fig. 2(d)]. Features at 3615.6 and 3618.7 eV are dominated by K (4s and 4p) with little contributions from N and O. The higher energy features again have mixed N and O contributions to the K-based molecular orbital (MO). These data indicate that for tightly bound bidentate

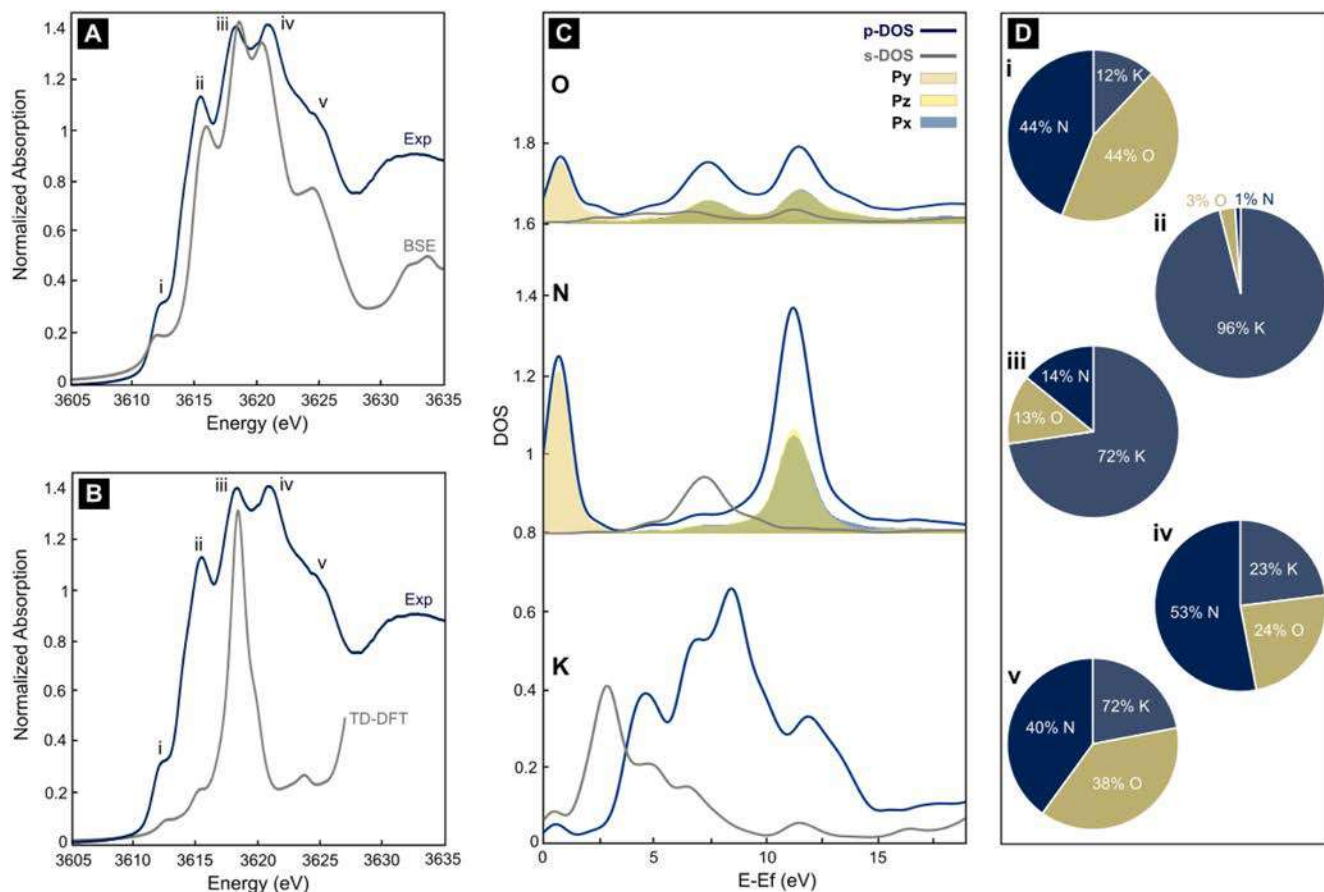


**FIG. 2.** Comparison of BSE (a) and TD-DFT (b) simulations of K-nitrate XANES spectrum (blue) and calculated spectrum (gray). (c) P and S density of states (DOS) in the presence of a core hole from BSE for K, N, and O. DOS plots up to 19 eV; feature at  $\sim 0.5$  eV in K DOS corresponds to feature i in the XAS spectrum; and feature at  $\sim 12.5$  eV in K p-DOS corresponds to feature v in (a). (d) MO contributions expressed as % for each feature in the TD-DFT spectrum.

ligands, such as  $\text{NO}_3^-$ , the K K-edge XAS spectra have strong contributions from bonding over a large energy range—starting from the lowest energy pre-edge feature (i) to features beyond the white line (iv and v).

Two spectra of  $\text{K}_3(\text{C}_6\text{H}_5\text{O}_7)\cdot\text{H}_2\text{O}$  were simulated starting from the monohydrate crystal structure and an anhydrous crystal structure (Fig. 3). The experimental spectrum is characterized by two relatively broad features separated by  $\sim 7$  eV. To lower energy, a weaker feature is apparent in the second derivative, although this pre-edge is shifted to higher energy by  $\sim 2$  eV compared to the  $\text{KNO}_3$  pre-edge (Fig. S3). OCEAN successfully calculates both intense features ii and iii; however, the relative intensity of the two peaks is estimated incorrectly for the anhydrous model [Fig. 3(a)]. The d-DOS contributes strongly to the lowest energy features (and results due to admixing of K 3d with K 4p) (Fig. S7). The relative intensity pattern becomes more agreeable with the experiment in the monohydrate model, indicating the possible impact of water on the higher energy feature. This is corroborated by both p- and s-DOS of H showing contributions to feature ii (Fig. S4), and O p-DOS has a strong contribution to feature iii [Fig. 3(c)]. Finally, BSE results

of both anhydrous and monohydrate models indicate the presence of a pre-edge, feature i, yet the intensity of this feature is greater in the anhydrous structure and shifted to a lower energy. Features in the K p-DOS [Fig. 3(c)] over  $\sim 1$  to 12 eV closely replicate the BSE spectrum [Fig. 3(a)]. The p-DOS associated with C and O contributes to all transitions marked in the experimental spectrum of  $\text{K}_3(\text{C}_6\text{H}_5\text{O}_7)\cdot\text{H}_2\text{O}$ , indicating the impact of K-citrate overlap over a wide energy range.

Potassium in  $\text{K}_3(\text{C}_6\text{H}_5\text{O}_7)\cdot\text{H}_2\text{O}$  and anhydrous  $\text{K}_3(\text{C}_6\text{H}_5\text{O}_7)$  crystallizes in more than one unique site in the crystal structure. Since the local structure affects TD-DFT calculations, we performed TD-DFT on each unique site in the crystal structure (Fig. S5; Table S1). The results show that the two structurally distinct monohydrate simulations are similar [Fig. S5(a)], while the spectral simulations for the anhydrous structure vary depending on which unique site is chosen. Therefore, the average of the calculated spectra was used for both the monohydrate and the anhydrous models [Fig. 3(b)]. The TD-DFT spectra of  $\text{K}_3(\text{C}_6\text{H}_5\text{O}_7)$  and  $\text{K}_3(\text{C}_6\text{H}_5\text{O}_7)\cdot\text{H}_2\text{O}$  simulate a low-energy pre-edge, feature i. This feature is shifted to a higher energy than the pre-edge feature in the TD-DFT spectrum of  $\text{KNO}_3$ ,

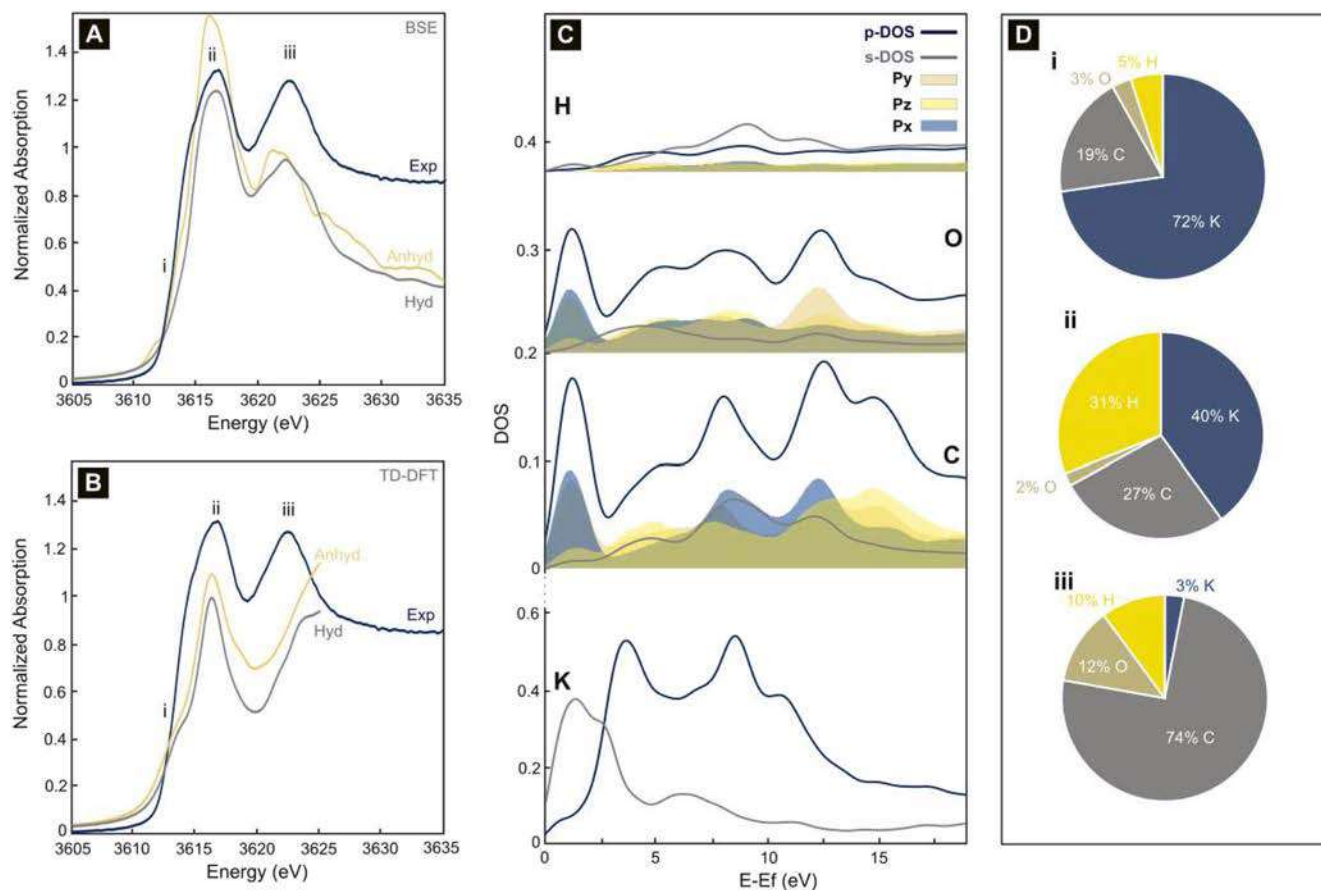


**FIG. 3.** Comparison of BSE (a) and TD-DFT (b) simulations of experimental K-citrate XANES spectrum (blue), including simulations of both monohydrate (gray) (tripotassium citrate monohydrate) and anhydrous (yellow). (c) P and S density of states (DOS) for tri-potassium citrate monohydrate in the presence of a core hole from BSE for K, C, O, and H. DOS plots up to 19 eV; feature at  $\sim 7.5$  eV in K p-DOS corresponds to feature ii in the XAS spectrum. (d) MO contributions expressed as % for each feature in the tripotassium citrate monohydrate TD-DFT spectrum.

similar to the second derivative in the experimental spectra. The higher energy feature centered around  $\sim 3622.6$  eV is poorly modeled both in energy position and in relative intensity compared to the lower energy feature centered around  $\sim 3617$  eV. However, like the BSE calculations, the monohydrate TD-DFT simulation better models the experimental relative intensities of the two features. If we consider only the hydrated structures, when K is 3-coordinated with an average bond distance of  $2.75$  Å, there is no feature within 2 eV of feature iii, while when K is 6-coordinated to O with an average bond distance of  $2.81$  Å, a feature is present (Table S1). Thus, both K coordination number and bond distance impact the energy position of the higher energy feature in  $K_3(C_6H_5O_7) \cdot H_2O$ . The lowest energy feature (i) is dominated by the C 2p character hybridized with K 4p, with minimal O and H contributions, while peak ii and iii have significantly more O and H contributions to the dominant molecular orbitals [Fig. 3(d)]. Here too, TD-DFT and BSE support one another, showing that the citrate has the greatest impact on the  $K_3(C_6H_5O_7) \cdot H_2O$  spectra, while the water contributes to higher energies.

Potassium complexed by water was simulated to understand the impact of  $H_2O$  coordination on a theoretically simulated spectrum (Fig. 4). We performed BSE simulations with an end-member single water coordinated to K model and a more realistic eight-water coordination model. The results reveal that upon going from a 1- to 8-water model, the spectrum starts from a single peak and becomes more complex. The DOS calculations for the 8-water [Fig. 4(b)] and 1-water (Fig. S6) models show a significant increase in the number of peaks and are indicative of decreased symmetry, which decreases the degeneracy in states involved in the XAS calculations. Furthermore, the calculated spectrum is strongly impacted by the core-hole, and hence, the p-DOS are not directly aligned with the calculated spectrum. TD-DFT simulations on both the 1-water and 8-water simulations show more realistic spectral simulations, particularly in comparison with a  $K^+$  in the solution spectrum.<sup>39,77</sup> Relative to the 1-water model, which is dominated by K 4p in the MOs [Fig. 4(c)], the 8-water model has significant contributions from hybridized K-water MOs in features ii, iii, and iv [Fig. 4(d)]. It is possible that the very low water contribution to the 1-water MOs is due to the



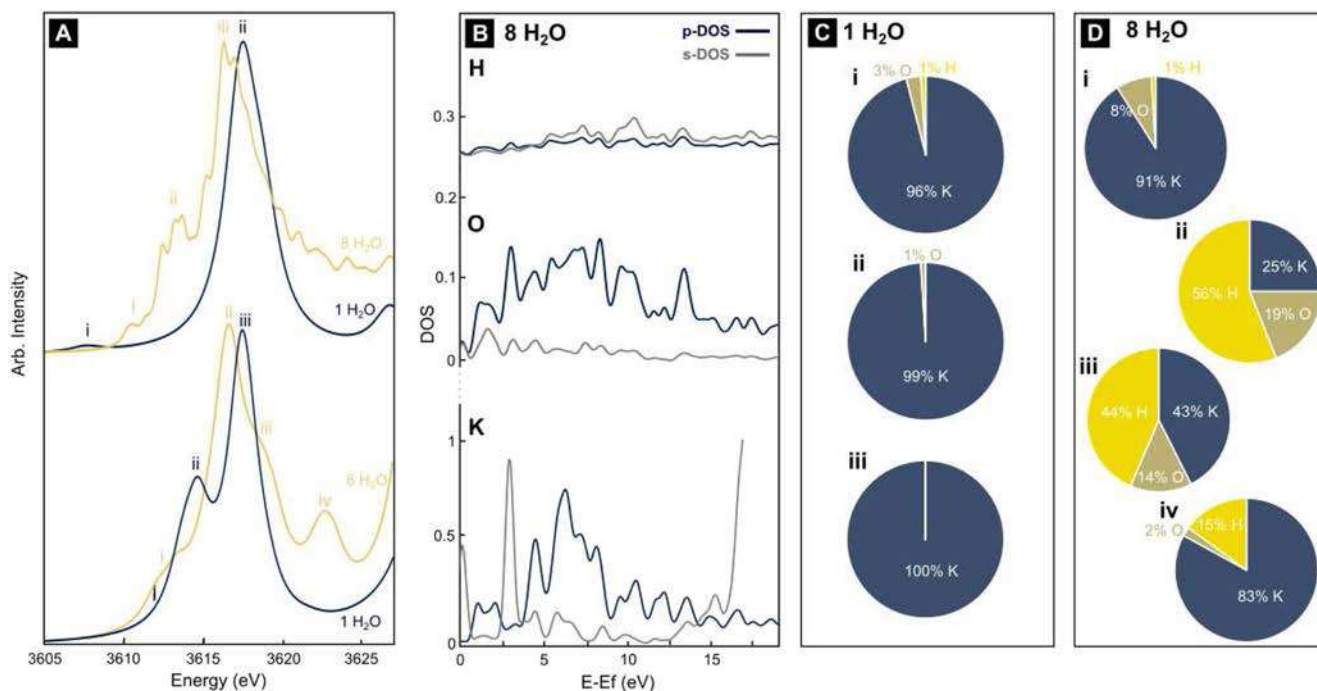


**FIG. 4.** (a) Comparison of BSE (top) and TD-DFT (bottom) simulations of K complexed by one H<sub>2</sub>O molecule (blue) or eight H<sub>2</sub>O molecules (yellow). (b) P and S density of states (DOS) for eight-H<sub>2</sub>O BSE simulation. Note that DOS for one H<sub>2</sub>O is omitted since it is an unrealistic complexation but can be found in the supplementary material. (c) and (d) MO contributions expressed as % for each feature in the TD-DFT spectrum for one and eight H<sub>2</sub>O molecules, respectively.

orientation of the water molecule relative to the K<sup>+</sup> ion in the optimized structural model. Nevertheless, the results indicate that K<sup>+</sup>-water based MOs have important contributions to the XANES spectra up to ~10 eV beyond the rising edge and support the results obtained for K<sub>3</sub>(C<sub>6</sub>H<sub>5</sub>O<sub>7</sub>)·H<sub>2</sub>O, where inclusion of the single water molecule in the model improves the spectral simulations.

## IV. DISCUSSION

### A. Extracting information from XANES and theory

XAS is an element-specific probe that provides information about the local structural and compositional environment of an absorbing atom. The lower-energy XANES region of XAS is impacted by a longer-range structure, especially in repeating structures such as those found in minerals. Theoretical methods, such as TD-DFT and BSE, can be used to simulate the structural and/or electronic transitions that give rise to the spectrum, providing detailed insights into the components that give rise to specific features. Typically, TD-DFT methods are more successful in simulating the lower-energy transitions, which are more localized to bound states. Plane wave based BSE multiple scattering methods are successful in simulating both the low energy features associated with localized or bound states and the post white-line spectral details associated with the itinerant or continuum states, although the plane wave BSE is more appropriate for periodic (crystalline) systems. This is generally shown to be true in our analysis, and by combining these complementary approaches, we successfully analyzed the measured

spectra. For example, for KNO<sub>3</sub>, which has a repeating structure with a single type of K and a bidentate ligand system, BSE is more accurate than TD-DFT. BSE reproduces five main transitions in the experimental spectrum [Fig. 2(a)]. While TD-DFT does not simulate the absolute intensities and is poorer to higher energies, the energy positions of the pre-edge features are more accurate than BSE.

The dipole selection rule for K K-edge XANES means that the spectra reflect transitions to final states with p-symmetry. However, our DFT calculations reveal that there is significant admixing of low-lying K 3d levels with 4p, especially the pre-edge features that have a strong mixing with NO<sub>3</sub><sup>-</sup> MOs. This shifts the transitions to lower energies relative to 4p transitions. This feature, which is lower in energy than any feature among the spectra shown here or reported in the literature,<sup>38,40,42</sup> reflects the unique pincer-like bonding between NO<sub>3</sub><sup>-</sup> and K<sup>+</sup>, and such low energy features may reflect similar bonding environments. Interestingly, a 1s- to 3d-based transition also exists in the rising edge of KCO<sub>2</sub>Me, which is shifted to higher energy and buried in the rising edge of the spectrum (Fig. 1). Both BSE and TD-DFT of K<sub>3</sub>(C<sub>6</sub>H<sub>5</sub>O<sub>7</sub>)·H<sub>2</sub>O reproduce this feature, although TD-DFT does a better job of simulating the energy position of this feature than BSE. In this case, the MOs associated with the transitions are dominated by C 2p and K 3d/4p levels. This indicates very little contribution from the first coordination ligand O and underscores the importance of the entire ligand to the bonding with K instead of only the first coordination. Such a feature on the rising edge has previously been observed in K-peptate.<sup>41</sup> In the case of

$\text{KNO}_3$ , MO hybridization also results in the high-energy feature (d) [Fig. 1(b)], which is absent in the other compounds. However, TD-DFT does not simulate its intensity well. This indicates that both MO-based transitions and long-range band structure contribute to this region. Yet, because K is coordinated with six  $\text{NO}_3^-$  ligands in the BSE calculation compared to one  $\text{NO}_3^-$  in the TD-DFT calculations, this could explain the difference in the simulated spectra. These results are consistent with a recent study of Prussian blue, a metal-cyanide, which shows the hybridization of K p-states with N and C (Mayer *et al.*, 2023). Together, the  $\sim 3612$  and  $\sim 3625$  eV features can be diagnostic of  $\text{NO}_3^-$  ligands in biological samples, especially given that no other K-organic or inorganic salts have a feature at 3625.0 eV (Schmidt *et al.*, 2022).

The potassium K-edge XANES spectra of  $\text{K}_2\text{CO}_3$  and  $\text{KHCO}_3$  have been reported and are similar to  $\text{K}_3(\text{C}_6\text{H}_5\text{O}_7)\cdot\text{H}_2\text{O}$  with two predominant peaks. Both have pre-edge features attributed to  $1s \rightarrow 3d$  transitions<sup>38,42</sup> hybridized with K 4p levels that appear to be more intense than those observed/assigned to  $\text{K}_3(\text{C}_6\text{H}_5\text{O}_7)\cdot\text{H}_2\text{O}$  herein. Davies *et al.* (2020) used multiple scattering-based methods to show that the energy position and intensity of the spectral features are dependent on cluster size, abundance of K in the structure, and expansion/contraction of the lattice. The dominantly assigned  $1s \rightarrow 3d$  and  $1s \rightarrow 4p$  features of  $\text{K}_2\text{CO}_3$  and  $\text{KHCO}_3$  have the same intensity, which is an unlikely situation and points to limitations of the multiple-scattering based methods in simulating the lower energy-bound state transitions. Here, the only control on the presence and energy position of the higher energy peak (iii) in  $\text{K}_3(\text{C}_6\text{H}_5\text{O}_7)\cdot\text{H}_2\text{O}$  is water and crystal orientation, which, in turn, impacts the K coordination.

Our calculations also reveal a key role of water coordination to the K. Results from K complexation with water molecules (Fig. 4) indicate that higher energy features are present with a greater number of water molecules. The source of these higher energy features is contributions from K hybridized with water-based orbitals, although with greater contributions from H. The simulated edge position also shifts to lower energy with increasing water molecules. This could be due to a change in the coordination number or due to an increase in average K–O first-shell distance from 2.65 to 2.77 upon increasing the number of water molecules from 1 to 8. A change in the K–O bond distance has been proposed as the shift in energy position of the white line in K-feldspar minerals compared to other K bearing minerals.<sup>78</sup> In addition, an increase in the K–K bond distance was observed in plane wave pseudopotential DFT calculations with the addition of  $\text{H}_2\text{O}$  added to the Prussian blue structure and also showed additional features to higher energy when K  $\text{H}_2\text{O}$  is present in the structure (Mayer *et al.*, 2023). A third reason can be seen in the increase in the water contribution to the K-based MOs responsible for the transition. This is evident from a comparison between the 1-water and the 8-water structure spectral features. Features i, ii, and iii arise from transitions to increasingly hybrid orbitals despite the fact that the K–O distances increase [Figs. 4(c) and 4(d)].

In summary, our results indicate that crystal packing and hydration, along with the unique molecular structures of K organic acid compounds, give rise to the rich spectral shapes with several well-separated transitions in the K K-edge XANES spectra. Theoretical methods, such as TD-DFT, which is sensitive to the pre-edge (lower-energy) and impacted by local bonding, and BSE, which is accurate at both low and higher energies but is more suited to

periodic systems, can successfully be used in conjunction to understand the K K-edge spectra in a holistic fashion.

## B. Implications for applied potassium XANES spectroscopy

An increasing number of research groups are applying K K-edge XANES spectroscopy to complex environmental systems, such as soils,<sup>42</sup> plants,<sup>41</sup> and biogenic marine carbonates.<sup>79,80</sup> Natural K-organic matter complexes are complicated and heterogeneous mixtures, evidenced by a number of K K-edge XANES spectra from biogenic material that display a similar single broad peak [e.g., K in humic acid (Fig. 1), K in fungal biomass,<sup>43</sup> and K in coral organic matrices<sup>79,80</sup>], and thus far, the bonding environment of K in these complexes remains elusive. The theoretical analyses in this study provide a molecular structure-based approach to understand the spectral transitions observed in K compounds, and this understanding can be applied to pare down the possible K-complexes in biological and environmental samples and ultimately obtain a smaller, relevant set of compounds that are present in the unknown K-organic matter.

The interpretation of the spectra of such unknown K-organic matter compounds necessitates a larger database of standards with K K-edge XANES of both K-organic matter and K-mineral systems and coupling of theoretical calculations on these compounds with linear combination analysis or (where possible) principal component analysis. However, the theoretical calculations presented here can be compared with K K-edge XANES of humic acid. Humic acid lacks most of the detailed features of the K-salts. The defining spectral characteristic is a broad set of transitions (with a maximum intensity at  $\sim 3618.8$  eV) and a sharp decrease in intensity following this feature. Our theoretical calculations indicate that the presence of water enhances the intensity to higher energy features, which are absent in the humic acid spectrum. However, there are similarities between humic acid and solvated K XANES spectra.<sup>39</sup> It is possible that solvated K is a component of humic acid, yet solvated K is the principal form of bioavailable K to plants. Understanding the differences in bonding environment between K-humic acid and solvated K is essential to our understanding of rhizosphere K cycling. In addition, the feature at 3618.8 eV in humic acid is shifted to a higher energy relative to the standards presented here, suggesting the presence of a dominant species with high intensity at this energy, or, it is possible that this main peak in humic acid is shifted to a higher energy due to, for example, bond distances such that K complexed to humic acid has different bond lengths than the first shell of the K-salts (typically in the range 2.8–2.88 Å based on crystal structures). Alternatively, there could be other ligands interacting in the K-humic acid complex since a majority of the K-salts studied here show mostly K–O–C contributions (with the exception of  $\text{KNO}_3$ ). Despite the growing literature using K K-edge XANES spectroscopy in environmental and biological samples, these studies employ a qualitative fingerprinting analysis,<sup>41,42,81</sup> which has its limitations. Theoretical molecular methods improve our fundamental understanding of complex and heterogeneous K K-edge XANES spectra in bio-environmental samples, particularly if the goal is to obtain a quantitative understanding of the mechanisms underlying K uptake, transformations, utilization, and storage.

## V. CONCLUSIONS

Potassium K-edge XANES data on several organic acid salts are presented, which show rich spectral diversity, despite having very similar bonding environments around the K center in these compounds (6–8 coordinates with the first shell O ligands). This opens the possibility that K K-edge XANES can be used as an important fingerprinting tool to understand K-coordination and binding in complex biological samples. A combination of both TD-DFT and BSE computational approaches was used for the detailed characterization of the electronic transitions that give rise to the unique features in two salts:  $\text{KNO}_3$  and  $\text{K}_3(\text{C}_6\text{H}_5\text{O}_7)\text{H}_2\text{O}$ . The results show that the K K-edge XANES spectra are sensitive to the extended ligand system, as opposed to being dominated by the first shell oxygen ligands. Weak water ligands are shown to have a strong impact on the spectral features as well, with their contribution showing up dominantly to higher energies [a second dominant feature of the  $\text{K}_3(\text{C}_6\text{H}_5\text{O}_7)\text{H}_2\text{O}$  spectrum]. This research holds promise in combining K K-edge XANES spectroscopy with synchrotron x-ray microscopy ( $\mu$ -XRF imaging) to study specific metabolic processes of plants and microbes in complex, heterogeneous systems, such as humic acid, and extending it to rhizosphere systems.

## SUPPLEMENTARY MATERIAL

Figures of crystal structures and additional theoretical calculations to support the results and discussion of this manuscript can be found in the online supplementary material.

## ACKNOWLEDGMENTS

The use of the Stanford Synchrotron Radiation Lightsource, SLAC National Accelerator Laboratory, was supported by the U.S. Department of Energy, Office of Science, Office of Basic Energy Sciences, under Contract No. DE-AC02-76SF00515. The SSRL Structural Molecular Biology Program is supported by the DOE Office of Biological and Environmental Research and the National Institutes of Health, National Institute of General Medical Sciences (Grant No. P30GM133894). A portion of this research was performed on a project award (10.46936/expl.proj.2021.60169/60008211) from the Environmental Molecular Sciences Laboratory, a DOE Office of Science User Facility, sponsored by the Biological and Environmental Research program under Contract No. DE-AC05-76RL01830. J.J.K. was supported by the Theory Institute for Materials and Energy Spectroscopies (TIMES) at SLAC, which is funded by the U.S. DOE, Office of Basic Energy Sciences, Division of Materials Sciences and Engineering, under Contract No. DE AC02-76SF0051.

## AUTHOR DECLARATIONS

### Conflict of Interest

The authors have no conflicts to disclose.

### Author Contributions

**Jocelyn A. Richardson:** Conceptualization (equal); Data curation (equal); Funding acquisition (equal); Project administration (supporting); Visualization (lead); Writing – original draft (lead);

Writing – review & editing (equal). **Hoshin Kim:** Data curation (equal); Formal analysis (equal); Methodology (lead); Resources (equal); Software (lead); Writing – original draft (equal); Writing – review & editing (equal). **Joshua J. Kas:** Data curation (equal); Formal analysis (equal); Methodology (lead); Resources (equal); Software (lead); Writing – original draft (equal); Writing – review & editing (equal). **Xiao You:** Formal analysis (supporting); Visualization (supporting); Writing – review & editing (equal). **Amity Andersen:** Resources (equal); Writing – review & editing (equal). **Bojana Ginovska:** Project administration (lead); Resources (lead); Supervision (lead); Writing – review & editing (equal). **Arunima Bhattacharjee:** Conceptualization (equal); Resources (equal); Writing – review & editing (equal). **Ritimukta Sarangi:** Conceptualization (equal); Funding acquisition (lead); Project administration (lead); Supervision (lead); Writing – original draft (supporting); Writing – review & editing (equal).

## DATA AVAILABILITY

The data that support the findings of this study are openly available in the Stanford Digital Repository at <https://purl.stanford.edu/fs421hj2342>.

## REFERENCES

- Y. Wang and W. H. Wu, “Potassium transport and signaling in higher plants,” *Annu. Rev. Plant Biol.* **64**, 451–476 (2013).
- C. Hafsi, A. Debez, and C. Abdely, “Potassium deficiency in plants: Effects and signaling cascades,” *Acta Physiol. Plant.* **36**(5), 1055–1070 (2014).
- A. Wakeel and M. Ishfaq, “Potassium in plants,” in *Potash Use and Dynamics in Agriculture* (Springer, 2022), pp. 19–27.
- M. U. Hassan, M. Aamer, M. Umer Chattha, M. Aman Ullah, S. Sulaman, M. Nawaz, W. Zhiqiang, M. Yanqin, and H. Guoqin, “The role of potassium in plants under drought stress: Mini review,” *J. Basic Appl. Sci.* **13**, 268–271 (2017).
- N. A. Mohd Zain and M. R. Ismail, “Effects of potassium rates and types on growth, leaf gas exchange and biochemical changes in rice (*Oryza sativa*) planted under cyclic water stress,” *Agric. Water Manage.* **164**, 83–90 (2016).
- Q. Xu, H. Fu, B. Zhu, H. A. Hussain, K. Zhang, X. Tian, M. Duan, X. Xie, and L. Wang, “Potassium improves drought stress tolerance in plants by affecting root morphology, root exudates, and microbial diversity,” *Metabolites* **11**(3), 131 (2021).
- D. L. Sparks, “Potassium dynamics in soils,” in *Advances in Soil Science* (1987), pp. 1–63.
- D. Britzke, L. S. da Silva, D. F. Moterle, D. dos Santos Rheinheimer, and E. C. Bortoluzzi, “A study of potassium dynamics and mineralogy in soils from subtropical Brazilian lowlands,” *J. Soils Sediments* **12**(2), 185–197 (2012).
- V. Römhald and E. A. Kirkby, “Research on potassium in agriculture: Needs and prospects,” *Plant Soil* **335**(1–2), 155–180 (2010).
- R. L. Mikkelsen, “Managing potassium for organic crop production,” *Horttechnology* **17**(4), 455–460 (2007).
- A. Sattar, M. Naveed, M. Ali, Z. A. Zahir, S. M. Nadeem, M. Yaseen, V. S. Meena, M. Farooq, R. Singh, M. Rahman, and H. N. Meena, “Perspectives of potassium solubilizing microbes in sustainable food production system: A review,” *Appl. Soil Ecol.* **133**, 146–159 (2019).
- F. Paris, B. Botton, and F. Lapeyrie, “In vitro weathering of phlogopite by ectomycorrhizal fungi: II. Effect of  $\text{K}^+$  and  $\text{Mg}^{2+}$  deficiency and N sources on accumulation of oxalate and  $\text{H}^+$ ,” *Plant Soil* **179**, 141 (1996).
- F. Paris, P. Bonnaud, J. Ranger, and F. Lapeyrie, “In vitro weathering of phlogopite by ectomycorrhizal fungi: I. Effect of  $\text{K}^+$  and  $\text{Mg}^{2+}$  deficiency on phyllosilicate evolution,” *Plant Soil* **177**(2), 191–201 (1995).

- <sup>14</sup>X. Hu, J. Chen, and J. Guo, "Two phosphate- and potassium-solubilizing bacteria isolated from Tianmu Mountain, Zhejiang, China," *World J. Microbiol. Biotechnol.* **22**(9), 983–990 (2006).
- <sup>15</sup>M. Song, I. Pedruzzi, Y. Peng, P. Li, J. Liu, and J. Yu, "K-extraction from muscovite by the isolated fungi," *Geomicrobiol. J.* **32**(9), 771–779 (2015).
- <sup>16</sup>X. Li, Y. Yin, S. Fan, X. Xu, E. Amombo, Y. Xie, and J. Fu, "Aspergillus aculeatus enhances potassium uptake and photosynthetic characteristics in perennial ryegrass by increasing potassium availability," *J. Appl. Microbiol.* **132**(1), 483–494 (2022).
- <sup>17</sup>B. Lian, B. Wang, M. Pan, C. Liu, and H. H. Teng, "Microbial release of potassium from K-bearing minerals by thermophilic fungus *Aspergillus fumigatus*," *Geochim. Cosmochim. Acta* **72**(1), 87–98 (2008).
- <sup>18</sup>F. Pinzari, J. Cuadros, A. D. Jungblut, J. Najorka, and E. Humphreys-Williams, "Fungal strategies of potassium extraction from silicates of different resistance as manifested in differential weathering and gene expression," *Geochim. Cosmochim. Acta* **316**, 168–200 (2022).
- <sup>19</sup>X. F. Sheng, "Growth promotion and increased potassium uptake of cotton and rape by a potassium releasing strain of *Bacillus edaphicus*," *Soil Biol. Biochem.* **37**(10), 1918–1922 (2005).
- <sup>20</sup>E. Hoffland, T. W. Kuyper, H. Wallander, C. Plassard, A. A. Gorbushina, K. Haselwandter, S. Holmström, R. Landeweert, U. S. Lundström, A. Rosling, R. Sen, M. M. Smits, P. A. W. Van Hees, and N. Van Breemen, "The role of fungi in weathering," *Front. Ecol. Environ.* **2**(5), 258–264 (2004).
- <sup>21</sup>R. Landeweert, E. Hoffland, R. D. Finlay, T. W. Kuyper, and N. Van Breemen, "Linking plants to rocks: Ectomycorrhizal fungi mobilize nutrients from minerals," *Trends Ecol. Evol.* **16**(5), 248–254 (2001).
- <sup>22</sup>J. Kirtzel, N. Ueberschaar, T. Deckert-Gaudig, K. Krause, V. Deckert, G. M. Gadd, and E. Kothe, "Organic acids, siderophores, enzymes and mechanical pressure for black slate bioweathering with the basidiomycete *Schizophyllum commune*," *Environ. Microbiol.* **22**(4), 1535–1546 (2020).
- <sup>23</sup>M. V. Dutton and C. S. Evans, "Oxalate production by fungi: Its role in pathogenicity and ecology in the soil environment," *Can. J. Microbiol.* **42**(9), 881–895 (1996).
- <sup>24</sup>G. M. Gadd, "Fungal production of citric and oxalic acid: Importance in metal speciation, physiology and biogeochemical processes," *Adv. Microb. Physiol.* **41**, 47–92 (1999).
- <sup>25</sup>M. Fomina, S. Hillier, J. M. Charnock, K. Melville, I. J. Alexander, and G. M. Gadd, "Role of oxalic acid overexcretion in transformations of toxic metal minerals by *Beauveria caledonica*," *Appl. Environ. Microbiol.* **71**(1), 371–381 (2005).
- <sup>26</sup>S. A. Welch and W. J. Ullman, "The effect of organic acids on plagioclase dissolution rates and stoichiometry," *Geochim. Cosmochim. Acta* **57**(12), 2725–2736 (1993).
- <sup>27</sup>A. Schmalenberger, A. L. Duran, A. W. Bray, J. Bridge, S. Bonneville, L. G. Benning, M. E. Romero-Gonzalez, J. R. Leake, and S. A. Banwart, "Oxalate secretion by ectomycorrhizal *Paxillus involutus* is mineral-specific and controls calcium weathering from minerals," *Sci. Rep.* **5**, 12187 (2015).
- <sup>28</sup>Z. b. Li, X. Lu, H. H. Teng, Y. Chen, L. Zhao, J. Ji, J. Chen, and L. Liu, "Specificity of low molecular weight organic acids on the release of elements from lizardite during fungal weathering," *Geochim. Cosmochim. Acta* **256**, 20–34 (2019).
- <sup>29</sup>C. Plassard and P. Fransson, "Regulation of low-molecular weight organic acid production in fungi," *Fungal Biol. Rev.* **23**(1–2), 30–39 (2009).
- <sup>30</sup>Z. Li, T. Bai, L. Dai, F. Wang, J. Tao, S. Meng, Y. Hu, S. Wang, and S. Hu, "A study of organic acid production in contrasts between two phosphate solubilizing fungi: *Penicillium oxalicum* and *Aspergillus niger*," *Sci. Rep.* **6**, 25313 (2016).
- <sup>31</sup>S. Bonneville, M. M. Smits, A. Brown, J. Harrington, J. R. Leake, R. Brydson, and L. G. Benning, "Plant-driven fungal weathering: Early stages of mineral alteration at the nanometer scale," *Geology* **37**(7), 615–618 (2009).
- <sup>32</sup>H. Wallander and T. Wickman, "Biotite and microcline as potassium sources in ectomycorrhizal and non-mycorrhizal *Pinus sylvestris* seedlings," *Mycorrhiza* **9**(1), 25–32 (1999).
- <sup>33</sup>G. Cibin, A. Mottana, A. Marcelli, and M. F. Brigatti, "Potassium coordination in trioctahedral micas investigated by K-edge XANES spectroscopy," *Mineral. Petrol.* **85**(1–2), 67–87 (2005).
- <sup>34</sup>M. F. Brigatti, D. Malferrari, M. Poppi, A. Mottana, G. Cibin, A. Marcelli, and G. Cinque, "Interlayer potassium and its neighboring atoms in micas: Crystal-chemical modeling and XANES spectroscopy," *Am. Mineral.* **93**(5–6), 821–830 (2008).
- <sup>35</sup>W. Xu, D. Chen, W. Chu, Z. Wu, A. Marcelli, A. Mottana, A. Soldatov, and M. F. Brigatti, "Quantitative local structure determination in mica crystals: *Ab initio* simulations of polarization XANES at the potassium K-edge," *J. Synchrotron Radiat.* **18**(3), 418–426 (2011).
- <sup>36</sup>C. Ragoen, L. Cormier, A.-I. Bidegaray, S. Vives, F. Henneman, N. Trcera, and S. Godet, "A XANES investigation of the network-modifier cations environment before and after the Na<sup>+</sup>/K<sup>+</sup> ion-exchange in silicate glasses," *J. Non-Cryst. Solids* **479**, 97–104 (2018).
- <sup>37</sup>G. Jacobs, V. R. R. Pendyala, M. Martinelli, W. D. Shafer, M. K. Gnanamani, S. Khalid, A. MacLennan, Y. Hu, and B. H. Davis, "Fischer-Tropsch synthesis: XANES spectra of potassium in promoted precipitated iron catalysts as a function of time on-stream," *Catal. Lett.* **147**(8), 1861–1870 (2017).
- <sup>38</sup>C. J. Davies, A. Mayer, J. Gabb, J. M. Walls, V. Degirmenci, P. B. J. Thompson, G. Cibin, S. Golunski, and S. A. Kondrat, "Operando potassium K-edge X-ray absorption spectroscopy: Investigating potassium catalysts during soot oxidation," *Phys. Chem. Chem. Phys.* **22**(34), 18976–18988 (2020).
- <sup>39</sup>A. J. Mayer, O. T. Beynon, A. J. Logsdail, K. G. U. Wijayantha, S. E. Dann, J. F. Marco, J. D. Elliott, M. Aramini, G. Cibin, and S. A. Kondrat, "Direct monitoring of the potassium charge carrier in Prussian blue cathodes using potassium K-edge X-ray absorption spectroscopy," *J. Mater. Chem. A* **11**(37), 19900–19913 (2023).
- <sup>40</sup>W. Li, X. M. Liu, and Y. Hu, "Potassium and calcium K-edge XANES in chemical compounds and minerals: Implications for geological phase identification," *Geostand. Geoanal. Res.* **44**(4), 805–819 (2020).
- <sup>41</sup>W. Li, X. M. Liu, Y. Hu, F. Z. Teng, Y. F. Hu, and O. A. Chadwick, "Potassium isotopic fractionation in a humid and an arid soil-plant system in Hawai'i," *Geoderma* **400**, 115219 (2021).
- <sup>42</sup>E. J. Schmidt, G. Zaroni, A. Bumgardner, B. Šegvić, K. Lewis, D. Abdala, and M. G. Siebecker, "Soil chemical extractions can alter potassium coordination in agricultural soils: A combined wet chemical and X-ray absorption spectroscopic approach," *Geoderma* **422**, 115914 (2022).
- <sup>43</sup>A. Bhattacharjee, O. Qafoku, J. A. Richardson, L. N. Anderson, K. Schwarz, L. M. Bramer, G. X. Lomas, D. J. Orton, Z. Zhu, M. H. Engelhard, M. E. Bowden, W. C. Nelson, A. Jumpponen, J. K. Jansson, K. S. Hofmoeckel, and C. R. Anderton, "A mineral-doped micromodel platform demonstrates fungal bridging of carbon hot spots and hyphal transport of mineral-derived nutrients," *mSystems* **7**(6), e0091322 (2022).
- <sup>44</sup>A. Bhattacharjee, D. Velickovic, J. A. Richardson, S. P. Couvillion, G. W. Vandergrift, O. Qafoku, M. J. Taylor, J. K. Jansson, K. Hofmoeckel, and C. R. Anderton, "Fungal organic acid uptake of mineral-derived K is dependent on distance from carbon hotspot," *MBio* **14**, e0095623 (2023).
- <sup>45</sup>K. Lopata, B. E. Van Kuiken, M. Khalil, and N. Govind, "Linear-response and real-time time-dependent density functional theory studies of core-level near-edge X-ray absorption," *J. Chem. Theory Comput.* **8**(9), 3284–3292 (2012).
- <sup>46</sup>J. J. Rehr and R. C. Albers, "Theoretical approaches to x-ray absorption fine structure," *Rev. Mod. Phys.* **72**(3), 621–654 (2000).
- <sup>47</sup>S. M. Webb, I. McNulty, C. Eyberger, and B. Lai, *AIP Conf. Proc.* **1365**, 196–199 (2011).
- <sup>48</sup>B. Ravel and M. Newville, *J. Synchrotron Radiat.* **12**, 537–541 (2005).
- <sup>49</sup>D. M. Burns and I. Iball, "Unit cells and space groups of citric acid and some potassium and sodium citrates," *Acta Crystallogr.* **7**(1), 137–138 (1954).
- <sup>50</sup>J. K. Nimmo and B. W. Lucas, "A neutron diffraction determination of the crystal structure of  $\alpha$ -phase potassium nitrate at 25 degrees C and 100 degrees C," *J. Phys. C: Solid State Phys.* **6**(2), 201–211 (1973).
- <sup>51</sup>W. L. Jorgensen, J. Chandrasekhar, J. D. Madura, R. W. Impey, and M. L. Klein, "Comparison of simple potential functions for simulating liquid water," *J. Chem. Phys.* **79**(2), 926–935 (1983).
- <sup>52</sup>I. S. Jeong and T. E. Cheatham, "Determination of alkali and halide monovalent ion parameters for use in explicitly solvated biomolecular simulations," *J. Phys. Chem. B* **112**(30), 9020–9041 (2008).
- <sup>53</sup>M. J. Abraham, D. van der Spoel, E. Lindahl, B. Hess, "GROMACS user manual version 2018," Royal Institute of Technology and Uppsala University.

- <sup>54</sup>H. J. C. Berendsen, J. P. M. Postma, W. F. van Gunsteren, A. DiNola, and J. R. Haak, "Molecular dynamics with coupling to an external bath," *J. Chem. Phys.* **81**(8), 3684–3690 (1984).
- <sup>55</sup>T. Darden, D. York, and L. Pedersen, "Particle mesh Ewald: An  $N$ -log( $N$ ) method for Ewald sums in large systems," *J. Chem. Phys.* **98**(12), 10089–10092 (1993).
- <sup>56</sup>B. Hess, H. Bekker, H. J. C. Berendsen, and J. G. E. M. Fraaije, "LINCS: A linear constraint solver for molecular simulations," *J. Comput. Chem.* **18**(12), 1463–1472 (1997).
- <sup>57</sup>D. R. Roe and T. E. Cheatham, "PTRAJ and CPPTRAJ: Software for processing and analysis of molecular dynamics trajectory data," *J. Chem. Theory Comput.* **9**(7), 3084–3095 (2013).
- <sup>58</sup>D. R. Roe and T. E. Cheatham, "Parallelization of CPPTRAJ enables large scale analysis of molecular dynamics trajectory data," *J. Comput. Chem.* **39**(25), 2110–2117 (2018).
- <sup>59</sup>D. S. Biovia, "Discovery studio modeling environment" (2015).
- <sup>60</sup>E. Aprà, E. J. Bylaska, W. A. de Jong, N. Govind, K. Kowalski, T. P. Straatsma, M. Valiev, H. J. J. van Dam, Y. Alexeev, J. Anchell, V. Anisimov, F. W. Aquino, R. Atta-Fynn, J. Autschbach, N. P. Bauman, J. C. Becca, D. E. Bernholdt, K. Bhaskaran-Nair, S. Bogatko, P. Borowski, J. Boschen, J. Brabec, A. Bruner, E. Cauei, Y. Chen, G. N. Chuev, C. J. Cramer, J. Daily, M. J. O. Deegan, T. H. Dunning, M. Dupuis, K. G. Dyall, G. I. Fann, S. A. Fischer, A. Fonari, H. Früchtl, L. Gagliardi, J. Garza, N. Gawande, S. Ghosh, K. Glaesemann, A. W. Götz, J. Hammond, V. Helms, E. D. Hermes, K. Hirao, S. Hirata, M. Jacquelin, L. Jensen, B. G. Johnson, H. Jönsson, R. A. Kendall, M. Klemm, R. Kobayashi, V. Konkov, S. Krishnamoorthy, M. Krishnan, Z. Lin, R. D. Lins, R. J. Littlefield, A. J. Logsdail, K. Lopata, W. Ma, A. V. Marenich, J. Martin del Campo, D. Mejia-Rodriguez, J. E. Moore, J. M. Mullin, T. Nakajima, D. R. Nascimento, J. A. Nichols, P. J. Nichols, J. Nieplocha, A. Otero-de-la-Roza, B. Palmer, A. Panyala, T. Pirojsirikul, B. Peng, R. Peverati, J. Pittner, L. Pollack, R. M. Richard, P. Sadayappan, G. C. Schatz, W. A. Shelton, D. W. Silverstein, D. M. A. Smith, T. A. Soares, D. Song, M. Swart, H. L. Taylor, G. S. Thomas, V. Tipparaju, D. G. Truhlar, K. Tsemekhman, T. Van Voorhis, Á. Vázquez-Mayagoitia, P. Verma, O. Villa, A. Vishnu, K. D. Vogiatzis, D. Wang, J. H. Weare, M. J. Williamson, T. L. Windus, K. Woliński, A. T. Wong, Q. Wu, C. Yang, Q. Yu, M. Zacharias, Z. Zhang, Y. Zhao, and R. J. Harrison, "NWChem: Past, present, and future," *J. Chem. Phys.* **152**(18), 184102 (2020).
- <sup>61</sup>C. Adamo and V. Barone, "Toward reliable density functional methods without adjustable parameters: The PBE0 model," *J. Chem. Phys.* **110**(13), 6158–6170 (1999).
- <sup>62</sup>S. Grimme, J. Antony, S. Ehrlich, and H. Krieg, "A consistent and accurate *ab initio* parametrization of density functional dispersion correction (DFT-D) for the 94 elements H-Pu," *J. Chem. Phys.* **132**(15), 154104 (2010).
- <sup>63</sup>M. Sekiya, T. Noro, T. Koga, and T. Shimazaki, "Relativistic segmented contraction basis sets with core-valence correlation effects for atoms  $_{57}\text{La}$  through  $_{71}\text{Lu}$ : Sapporo-DK- $n$ ZP sets ( $n = \text{D, T, Q}$ )," *Theor. Chem. Acc.* **131**(7), 1247 (2012).
- <sup>64</sup>T. Noro, M. Sekiya, and T. Koga, "Segmented contracted basis sets for atoms H through Xe: Sapporo-(DK)- $n$ ZP sets ( $n = \text{D, T, Q}$ )," *Theor. Chem. Acc.* **131**(2), 1124 (2012).
- <sup>65</sup>T. H. Dunning, "Gaussian basis sets for use in correlated molecular calculations. I. The atoms boron through neon and hydrogen," *J. Chem. Phys.* **90**(2), 1007–1023 (1989).
- <sup>66</sup>L. Skripnikov, "Chemissian version 4.4.3, visualization computer program" (2016).
- <sup>67</sup>J. Vinson, J. J. Rehr, J. J. Kas, and E. L. Shirley, "Bethe-Salpeter equation calculations of core excitation spectra," *Phys. Rev. B* **83**(11), 115106 (2011).
- <sup>68</sup>P. Giannozzi, S. Baroni, N. Bonini, M. Calandra, R. Car, C. Cavazzoni, D. Ceresoli, G. L. Chiarotti, M. Cococcioni, I. Dabo, A. Dal Corso, S. de Gironcoli, S. Fabris, G. Fratesi, R. Gebauer, U. Gerstmann, C. Gougoussis, A. Kokalj, M. Lazzeri, L. Martin-Samos, N. Marzari, F. Mauri, R. Mazzarello, S. Paolini, A. Pasquarello, L. Paulatto, C. Sbraccia, S. Scandolo, G. Sclauzero, A. P. Seitsonen, A. Smogunov, P. Umari, and R. M. Wentzcovitch, "QUANTUM ESPRESSO: A modular and open-source software project for quantum simulations of materials," *J. Phys.: Condens. Matter* **21**(39), 395502 (2009).
- <sup>69</sup>P. Giannozzi, O. Andreussi, T. Brumme, O. Bunau, M. Buongiorno Nardelli, M. Calandra, R. Car, C. Cavazzoni, D. Ceresoli, M. Cococcioni, N. Colonna, I. Carnimeo, A. Dal Corso, S. de Gironcoli, P. Delugas, R. A. DiStasio, A. Ferretti, A. Floris, G. Fratesi, G. Fugallo, R. Gebauer, U. Gerstmann, F. Giustino, T. Gorni, J. Jia, M. Kawamura, H.-Y. Ko, A. Kokalj, E. Küçükbenli, M. Lazzeri, M. Marsili, N. Marzari, F. Mauri, N. L. Nguyen, H.-V. Nguyen, A. Otero-de-la-Roza, L. Paulatto, S. Poncè, D. Rocca, R. Sabatini, B. Santra, M. Schlipf, A. P. Seitsonen, A. Smogunov, I. Timrov, T. Thonhauser, P. Umari, N. Vast, X. Wu, and S. Baroni, "Advanced capabilities for materials modelling with QUANTUM ESPRESSO," *J. Phys.: Condens. Matter* **29**(46), 465901 (2017).
- <sup>70</sup>P. Giannozzi, O. Baseggio, P. Bonfà, D. Brunato, R. Car, I. Carnimeo, C. Cavazzoni, S. de Gironcoli, P. Delugas, F. Ferrari Ruffino, A. Ferretti, N. Marzari, I. Timrov, A. Urru, and S. Baroni, "Quantum ESPRESSO toward the exascale," *J. Chem. Phys.* **152**(15), 154105 (2020).
- <sup>71</sup>J. P. Perdew and Y. Wang, "Accurate and simple analytic representation of the electron-gas correlation energy," *Phys. Rev. B* **45**(23), 13244–13249 (1992).
- <sup>72</sup>M. J. van Setten, M. Giantomassi, E. Bousquet, M. J. Verstraete, D. R. Hamann, X. Gonze, and G.-M. Rignanese, "The PSEUDODOJO: Training and grading a 85 element optimized norm-conserving pseudopotential table," *Comput. Phys. Commun.* **226**, 39–54 (2018).
- <sup>73</sup>G. Kresse and J. Hafner, "*Ab initio* molecular dynamics for liquid metals," *Phys. Rev. B* **47**(1), 558–561 (1993).
- <sup>74</sup>G. Kresse and J. Furthmüller, "Efficiency of *ab-initio* total energy calculations for metals and semiconductors using a plane-wave basis set," *Comput. Mater. Sci.* **6**(1), 15–50 (1996).
- <sup>75</sup>G. Kresse and J. Furthmüller, "Software VASP, vienna (1999)," *Phys. Rev. B* **54**(11), 169 (1996).
- <sup>76</sup>G. Kresse and D. Joubert, "From ultrasoft pseudopotentials to the projector augmented-wave method," *Phys. Rev. B* **59**(3), 1758 (1999).
- <sup>77</sup>H. W. Huang, S. H. Hunter, W. K. Warburton, and S. C. Moss, "X-ray absorption edge fine structure of potassium ions in various environments: Application to frog blood cells," *Science* **204**(4389), 191–193 (1979).
- <sup>78</sup>C. L. Spiro, J. Wong, F. W. Lytle, R. B. Gregor, D. H. Maylotte, and S. H. Lamson, "Forms of potassium in coal and its combustion products," *Fuel* **65**(3), 327–336 (1986).
- <sup>79</sup>W. Li, X. M. Liu, K. Wang, F. J. Fodrie, T. Yoshimura, and Y. F. Hu, "Potassium phases and isotopic composition in modern marine biogenic carbonates," *Geochim. Cosmochim. Acta* **304**, 364–380 (2021).
- <sup>80</sup>W. Li, X. M. Liu, K. Wang, Y. Hu, A. Suzuki, and T. Yoshimura, "Potassium incorporation and isotope fractionation in cultured scleractinian corals," *Earth Planet. Sci. Lett.* **581**, 117393 (2022).
- <sup>81</sup>J. Richardson, C. Anderton, and A. Bhattacharjee, "Saprotrophic fungus induces microscale mineral weathering to source potassium in a carbon-limited environment," *Minerals* **13**(5), 641 (2023).